Macromolecules

pubs.acs.org/Macromolecules Article

Secondary Structures of Polypeptide-Based Diblock Copolymers Influence the Microphase Separation of Templates for the Fabrication of Microporous Carbons

Ahmed F. M. EL-Mahdy,* Tzu Ching Yu, Mohamed Gamal Mohamed, and Shiao-Wei Kuo*

Cite This: *Macromolecules* 2021, 54, 1030−1042 Read Online

ACCESS | Metrics & More | Article Recommendations | Supporting Information

ABSTRACT: In this study, we synthesized two forms of the polypeptide-based rod−coil diblock copolymer poly(ethylene oxide-*b*-*γ*-benzyl-L-glutamate) (PEO-*b*-PBLG), comprising hydrophilic PEO as the coil segment and hydrophobic PBLG as the rod segment, with different degrees of polymerization (DPs) of the PBLG segment (DP = 20 and 45), through ring-opening polymerization of *N*-carboxyanhydride with amino-terminated PEO as the macroinitiator. Fourier transform infrared (FTIR) spectroscopy revealed the secondary structures of the resultant PEO-*b*-PBLG block copolymers with an *α*-helical conformation, while wide-angle X-ray diffraction (WAXD) revealed a hexagonally packed cylinder structure for the PBLG segments. When we blended the diblock copolymers with a resol-type phenolic resin at various compositions, FTIR spectra suggested that the resol OH groups preferred to hydrogen-bond with the ether oxygen atoms of the PEO segment, rather than with the C═O groups of the PBLG segment. At high resol contents, the crystalline structure of the PEO segment was destroyed, while the *α*-helical conformation and hexagonal cylinder structure of the PBLG segment remained unchanged, as determined using differential scanning calorimetry, FTIR spectroscopy, and WAXD. We prepared a series of microporous carbons through thermal calcination of resol/PEO-*b*-PBLG blends at various compositions. The microstructures of the resulting carbons were strongly influenced by the secondary structure of the PBLG segments, rather than the microphase separation of the block segments, in the resol/PEO *b*-PBLG blends. These microporous carbons exhibited an extremely high supercapacitor performance, with massive specific capacitances (up to 758.4 F g^{-1} at a current density of 0.5 A g^{-1}) and excellent stabilities (up to 97.32% after 2000 cycles at a current density of 10 A g^{-1}).

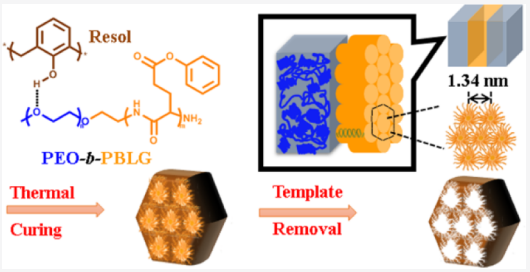

INTRODUCTION

The rapid development of electronics and electric transportation has spurred research into durable and renewable energy storage and conversion devices.[1−3] Supercapacitors—especially, electrical double-layer capacitors (EDLCs)—are among the most widely used energy storage devices because of their ultralong cyclic lives, high power densities, low-cost maintenance, and environmentally friendly compositions.[4−6] Supercapacitors have been applied in a wide range of applications, including fuel cells, portable electric equipment, lead-acid batteries, uninterruptable power sources, medical devices, and lithium-ion batteries.[7−14] The energy storage efficiency of a supercapacitor, especially an EDLC, depends strongly on the nature of its electrode materials. Porous carbonaceous materials are often used as electrode materials because they provide high electrical conductivities, large surface areas, and outstanding structural tenability, thereby enhancing the adsorption and transfer of anions and cations at the interface between the electrolyte and the electrode.[15−17] Industrially, activated carbons have been the most popular EDLC electrode materials; in the laboratory, several other porous materials (e.g., graphenes, templated carbons, carbide-derived carbons, and hierarchical porous carbons[18−21]), as well as conjugated microporous polymers, covalent triazine-based frameworks, covalent organic frameworks, and metal organic frameworks, have been developed as promising electrode materials.[22−31]

The physicochemical properties of carbonaceous electrode materials and the efficiencies of their corresponding supercapacitors are strongly influenced by the nature of their carbon sources and their synthesis strategies.[32,33] The carbon sources of most porous carbon materials were initially obtained from fossil sources (e.g., coal and bones), even though such sources have obvious shortcomings. For example, carbons obtained from the pyrolysis of coal generally contain huge amounts of impurities and their purification can be complicated and costly.[34] Therefore, the quest remains to find highly pure and effective carbon sources that can enhance the energy storage efficiency. Chemical and physical synthetic strategies toward

Received: July 28, 2020
Revised: October 10, 2020
Published: November 19, 2020

https://dx.doi.org/10.1021/acs.macromol.0c01748
Macromolecules 2021, 54, 1030−1042

Scheme 1. (a) Synthesis of Resol; (b) Chemical Structure of mPEO-NH_2; (c) Synthesis of the PEO-*b*-PBLG Diblock Copolymers; and (d) Hydrogen Bonding in Resol/PEO-*b*-PBLG Blends

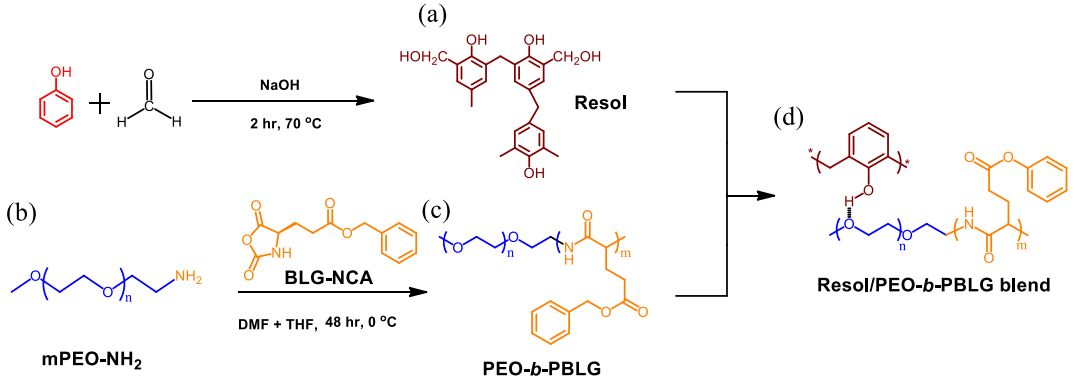

porous carbon materials have also been developed as promising alternatives to fossil-based carbons. Several intriguing synthetic approaches have been used to obtain high-quality carbon materials, including excimer laser ablation of graphitic targets, carbonization of organic/polymeric precursors, arc discharge syntheses, chemical vapor deposition, chemical methods, and sputtering/plasma-based syntheses.[35−39] Nevertheless, these methods can require harsh conditions, and the resulting ultra-microporosity can cause desolvated electrolyte ions to be positioned too close to the electrode surface, thereby decreasing the thickness of the electrode in the EDLC and lowering the capacitance efficiency.[40]

Block copolymers comprise at least two polymer segments connected together through covalent bonds. One of the attractive characteristics of block copolymers is that they can display microphase separation resulting in self-assembly into various morphologies.[41−43] The use of block copolymers as soft templates for the preparation of microporous, mesoporous, and even macroporous materials has received much attention for a diverse array of applications, including nanotechnology, drug delivery, photonic crystals, and energy storage.[44−46] A common strategy for the fabrication of porous carbons from block copolymers involves organic−organic self-assembly of the block copolymer as a structure-directing agent with a phenolic resin as a carbon source.[47,48] The triblock copolymer Pluronic F127, a noninoic hydrophilic surfactant comprising two hydrophilic polyethylene (PEO) segments and one hydrophobic polypropylene (PPO) segment, has been used widely as a structure-directing agent for the preparation of such porous carbons.[49−55] Pluronic F127 has been applied in the fabrication of various kinds of porous carbons through its assembly with phenolic resins or other natural carbon precursors (e.g., melamine−formaldehyde resin, resorcinol resin, polypyrrole, starch, lignin, and fructose).[49−55] Nevertheless, use of the F127 triblock copolymer is restricted in its ability to tune the arrangement and size of the pores; accordingly, other PEO-based block copolymers have also been employed, including PEO-*b*-PS, PEO-*b*-PMMA, PEO-*b*-PCL, and PEO-*b*-PLA, which can be classified as coil−coil diblock copolymers.[56−67] Using typical PEO-based coil−coil diblock copolymers as templates readily provides mesoporous materials (pore size > 2 nm) displaying long-range order.[56−67]

In addition to coil−coil diblock copolymers, rod−coil diblock copolymers composed entirely of rigid-rod and flexible-coil blocks generally form unique self-assembled nanostructures induced by several noncovalent interactions (e.g., electrostatic interactions, hydrogen bonding, and hydrophobic and hydrophilic effects). The microphase separation of the rod and coil blocks and the resulting formation of their various anisotropic structures are mainly controlled by such factors.[68−72] Rod blocks have been studied widely; they generally undergo phase separation into nematic or layered smectic structures.[73,74] Among the synthetic rod polymers, those with helical and rod structures are attractive because their secondary structures can be highly stabilized through intramolecular and/or intermolecular interactions. Polypeptides are widely investigated types of helical and rod polymers, in which their α-helical secondary structures be forced to the rod structure. This rod structure of a polypeptide controls the formation of lyotropic and thermotropic crystalline phases.[75−77] We suspected that the incorporation of a coil block (e.g., a PEO segment) into a helical rod polypeptide [e.g., poly (γ-benzyl-L-glutamate) (PBLG)] would form a helical rod−coil block copolymer that could be used as a soft template to prepare interesting porous materials.

In this study, we synthesized two poly(ethylene oxide-*b*-γ-benzyl-L-glutamate) (PEO-*b*-PBLG) rod−coil diblock copolymers—PEO_{114}-*b*-$PBLG_{20}$ and PEO_{114}-*b*-$PBLG_{45}$—as soft templates through simple ring-opening polymerization (ROP) using amino-terminated PEO (mPEO-NH_2) as an initiator (Scheme 1). The chemical structures and molecular weights of the copolymers and the secondary structures of their PBLG segments were determined using Fourier transform infrared (FTIR) spectroscopy, nuclear magnetic resonance (NMR) spectroscopy, gel permeation chromatography (GPC), and wide-angle X-ray diffraction (WAXD). We blended these PEO-*b*-PBLG diblock copolymers with a resol-type phenolic resin at various compositions (Scheme 1). We used FTIR spectroscopy, WAXD, and differential scanning calorimetry (DSC) to investigate the hydrogen bonding interactions, secondary structures, and microphase separation of these resol/PEO-*b*-PBLG blends. Finally, we prepared microporous carbons from the PEO-*b*-PBLG diblock copolymers as soft templates and resol as the carbon source (Scheme 2). We used thermogravimetric analysis (TGA), N_2 sorption isotherms, WAXD, and transmission electron microscopy (TEM) to evaluate the characteristics of these microporous carbons. Because of their high surface areas and microphase structures, the synthesized microporous carbons displayed an excellent performance for energy storage applications.

https://dx.doi.org/10.1021/acs.macromol.0c01748
Macromolecules 2021, 54, 1030−1042

Scheme 2. (a) Schematic Representation of the Chemical Structure of a PEO-*b*-PBLG Rod−Coil Diblock Copolymer: PEO Coils with a Crystalline Domain and PBLG Rods Aligned Parallel to the Normal Layer of PEO with a Hexagonal Packed Cylinder Spacing of 1.34 nm; (b) Microphase Separation of the Self-Assembled Structure in Resol/PEO-*b*-PBLG Blends; and (c) Preparation of a Microporous Carbon after Thermal Curing of the Resol Resin and Subsequent Removal of the Templating PEO-*b*-PBLG Diblock Copolymer

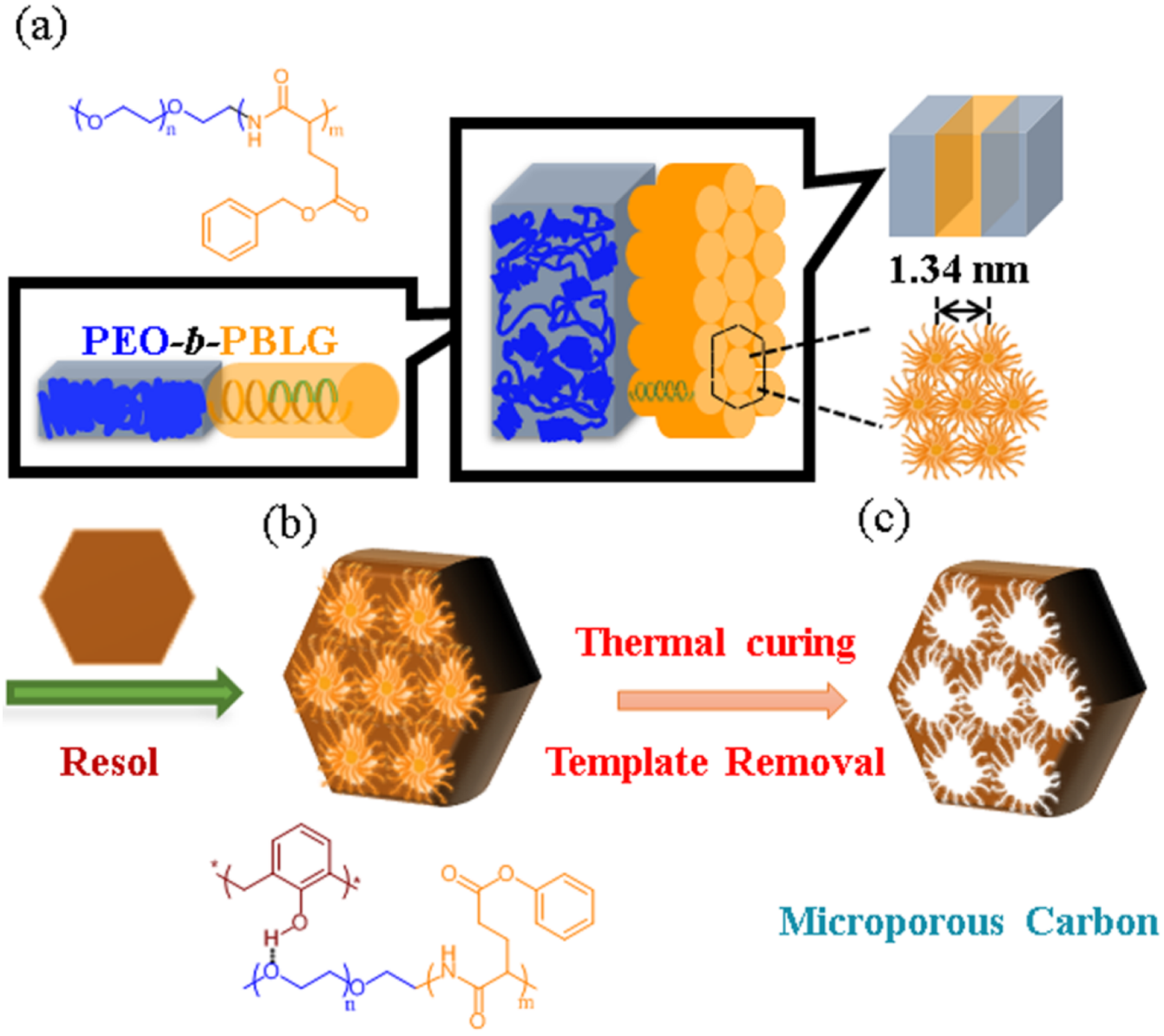

EXPERIMENTAL SECTION

Materials. Trimethylamine, L-glutamic acid, *tert*-butanol, benzyl alcohol, sodium bicarbonate, and triphosgene were obtained from Alfa Aesar. Amino-terminated mPEO-NH_2 (M_n = 5000 g/mol) (Scheme 1b) was purchased from Sigma-Aldrich. MeOH, EtOAc, *N*,*N*-dimethylformamide, sulfuric acid, and EtOH were used as received. Benzyl L-glutamate *N*-carboxyanhydride (BLG-NCA)[78] and resol-type phenolic resin were synthesized using procedures described previously (Scheme 1a and Figure S1).[61,65]

PEO-*b*-PBLG Diblock Copolymers. The PEO-*b*-PBLG diblock copolymers were synthesized from the monomer BLG-NCA through ROP using mPEO-NH_2 as the initiator (Scheme 1c). The mPEO-NH_2 was placed in a flask connected to the vacuum line, dimethylformamide (DMF) was added via a syringe, and then, different amounts of the monomer BLG-NCA were introduced. The PEO-*b*-PBLG diblock copolymer was precipitated from the solution at 0 °C for 24 h in cold MeOH. The precipitate was dissolved in DMF and precipitated from cold MeOH again. The PEO-*b*-PBLG diblock copolymer was purified three times from MeOH/diethyl ether to give a pure white powder. The sample was dried at 40 °C in a vacuum oven (yield: 80%). The physical properties of the two different PEO-*b*-PBLG block copolymers are summarized in Table 1.

Microporous Carbons from Resol/PEO-*b*-PBLG Blends. Different amounts of resol/PEO-*b*-PBLG blends (Table S1) were dissolved in tetrahydrofuran (blend composition: 5 wt %) until the solutions become transparent and homogeneous. The solution was

Table 1. Physical Characterization Data for the PEO-*b*-PBLG Block Copolymers Synthesized in This Study

polymers	M_n (^{1}H NMR, Da)	PDI (GPC)	T_m (°C)
PEO_{114}-*b*-$PBLG_{20}$	9700	1.10	58.3
PEO_{114}-*b*-$PBLG_{45}$	16,100	1.09	59.0

https://dx.doi.org/10.1021/acs.macromol.0c01748
Macromolecules 2021, 54, 1030−1042

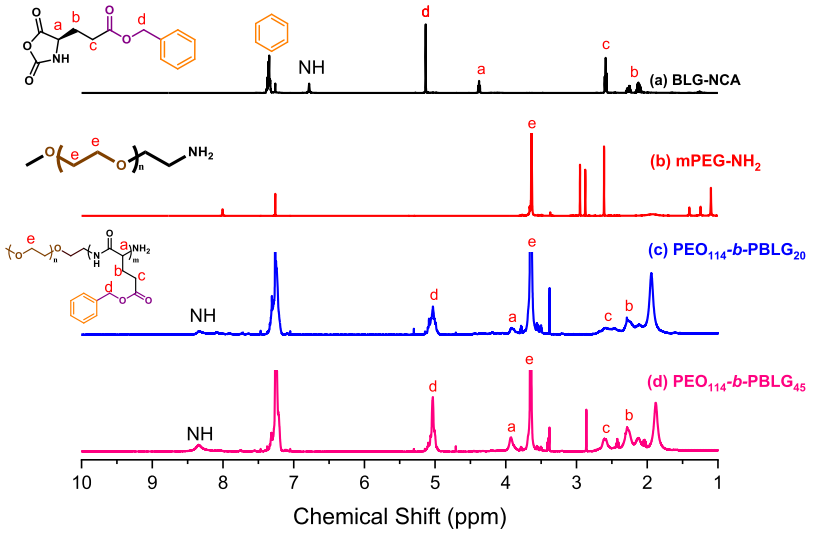

Figure 1. ^{1}H NMR spectra of (a) BLG-NCA, (b) mPEO-NH_2, (c) PEO_{114}-*b*-$PBLG_{20}$, and (d) PEO_{114}-*b*-$PBLG_{45}$ in $CDCl_3$ containing 15% trifluoroacetyl.

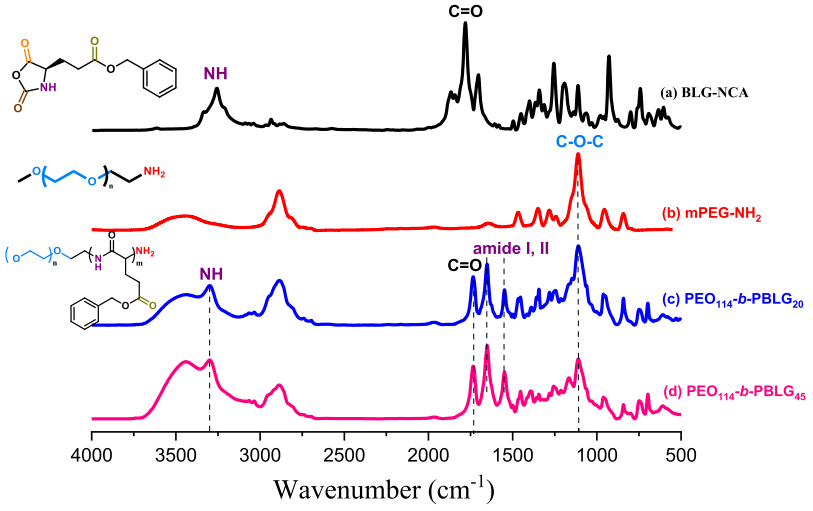

Figure 2. FTIR spectra of (a) BLG-NCA, (b) mPEO-NH_2, (c) PEO_{114}-*b*-$PBLG_{20}$, and (d) PEO_{114}-*b*-$PBLG_{45}$.

poured into a Teflon dish and the solvent was evaporated at 30 °C for 10 h (evaporation-induced self-assembly). The solid compound was heated at a heating rate of 1 °C/min up to 150 °C and then left at that temperature for 24 h. Pyrolysis of the PEO-*b*-PBLG diblock copolymer was performed at 420 °C for 6 h (based on TGA); the microporous carbons from resol/PEO-*b*-PBLG = 50/50, 60/40, and 70/30 blends were provided after further heating at 700 °C for 3 h in a tubular furnace under a N_2 atmosphere (Scheme 2).

RESULTS AND DISCUSSION

PEO-*b*-PBLG Diblock Copolymers. We synthesized two PEO-*b*-PBLG diblock copolymers through NCA ROP (Scheme 1c). PBLG block segments having two different molecular weights were obtained using amino-terminated PEO (mPEO-NH_2) as the macroinitiator. We used ^{1}H NMR spectroscopy to determine the molecular weights of the two PEO-*b*-PBLG diblock copolymers. For the BLG monomer, multiple signals appeared at 7.31−7.38 ppm for the aromatic protons, a singlet appeared at 6.40 ppm for the NH proton, and a signal appeared at 5.12 ppm for the methylene protons; other peaks are assigned in Figure 1a. The spectrum of mPEO-NH_2 featured a signal at 3.65 ppm [peak (e)] for the

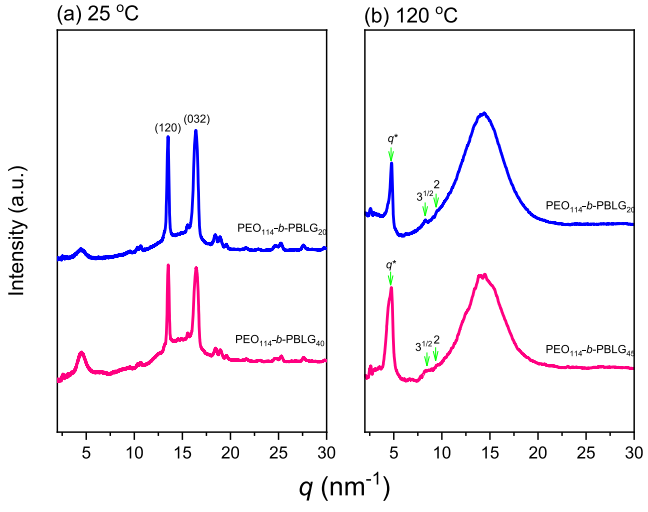

Figure 3. WAXD patterns of PEO_{114}-*b*-$PBLG_{20}$ and PEO_{114}-*b*-$PBLG_{45}$ diblock copolymers recorded at (a) 25 and (b) 120 °C.

https://dx.doi.org/10.1021/acs.macromol.0c01748
Macromolecules 2021, 54, 1030−1042

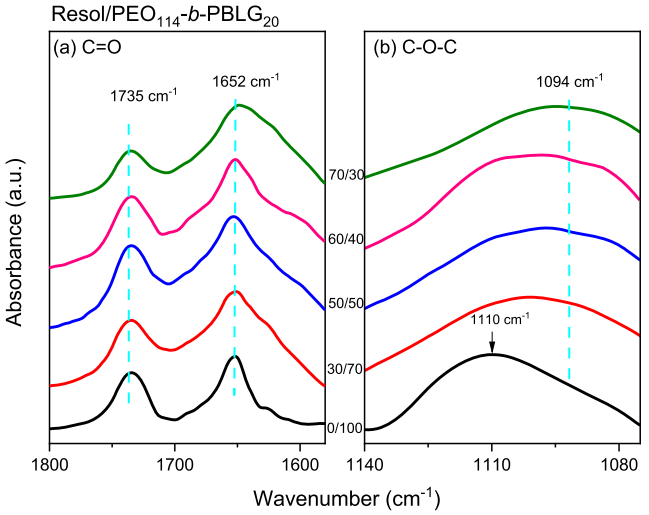

Figure 4. FTIR spectra of resol/PEO_{114}-*b*-$PBLG_{20}$ blends of various compositions: (a) C═O and (b) C−O−C stretching regions recorded at room temperature.

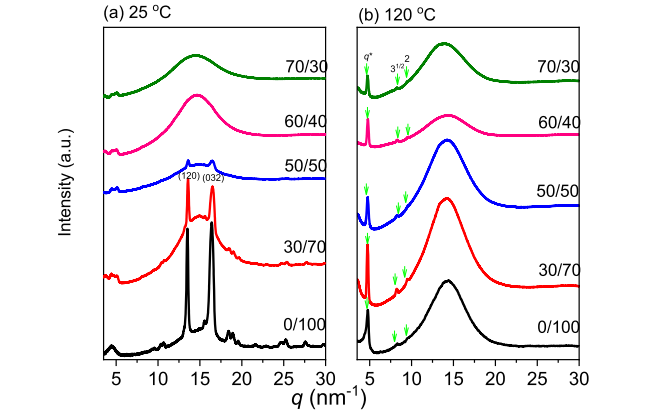

Figure 5. WAXD patterns of resol/PEO_{114}-*b*-$PBLG_{20}$ blends of various compositions recorded at (a) 25 and (b) 120 °C.

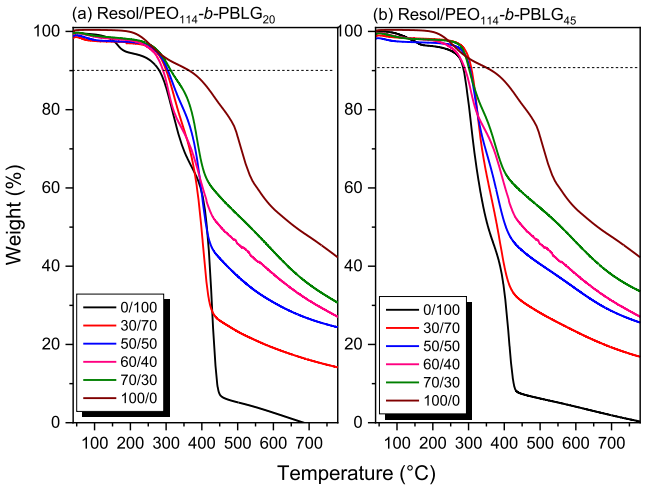

Figure 6. TGA thermograms of microporous carbons obtained after calcination of (a) resol/PEO_{114}-*b*-$PBLG_{20}$ and (b) resol/PEO_{114}-*b*-$PBLG_{45}$ blends of various compositions.

methylene units of the PEO segment (Figure 1b). Figure 1c,d displays the ^{1}H NMR spectra of the PEO-*b*-PBLG block

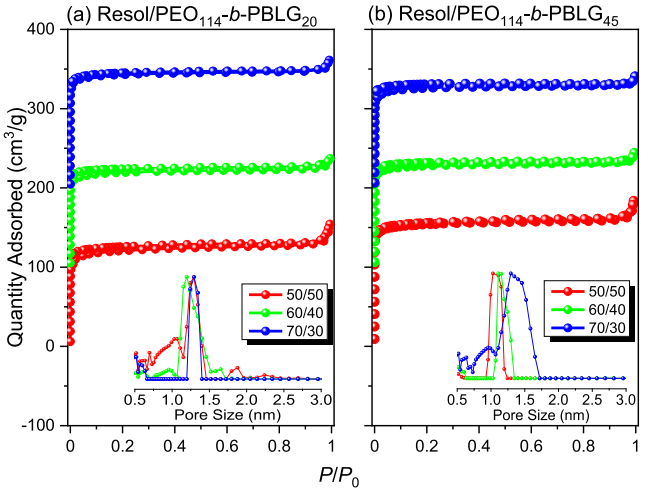

Figure 7. Nitrogen adsorption/desorption isotherms of microporous carbons obtained after calcination of (a) resol/PEO_{114}-*b*-$PBLG_{20}$ and (b) resol/PEO_{114}-*b*-$PBLG_{45}$ blends of various compositions. Insets: NLDFT pore-size distributions of the corresponding microporous carbons.

copolymers featuring the PBLG segments of two different molecular weights. After NCA ROP, the signal for the NH proton had shifted downfield from 6.40 ppm (for BLG) to 8.32 ppm and the signal of the methine proton [peak (a)] had shifted to highfield from 4.37 ppm (for BLG) to 3.90 ppm; the positions of the other signals were close to those of the BLG monomer, as assigned in Figure 1c,d. We calculated the molecular weights of the PEO-*b*-PBLG block copolymers from the ratio of peak (e) (from the PEO segment) to peak (d) (from the PBLG segment). Table 1 summarizes the properties of the PEO-*b*-PBLG diblock copolymers determined from their ^{1}H NMR spectra and GPC traces.

Figure 2 presents FTIR spectra of the BLG monomer, mPEO-NH_2, and PEO-*b*-PBLG diblock copolymers measured at room temperature. The spectrum of BLG featured absorption signals at 1720, 1785, and 1882 cm^{-1} corresponding to the side chain C═O and anhydride units; the signal for the NH units appeared at 3250 cm^{-1} (Figure 2a). The spectrum of mPEO-NH_2 featured an absorption signal at 1110 cm^{-1} representing the C−O−C stretching of the PEO segment (Figure 2b). The FTIR spectra of the PEO-*b*-PBLG diblock copolymers displayed two new absorptions at 1652 and 1550 cm^{-1} corresponding to the amide I and II absorptions of their PBLG segments, respectively; in addition, the signal of the side chain C═O units of the PBLG segments had shifted to 1734 cm^{-1} after NCA ROP of the BLG monomer (Figure 2c,d). The amide I band at 1652 cm^{-1} is characteristic of an α-helical secondary structure; we did not observe signals for the β-sheet conformation (near 1627 cm^{-1}) or the β-turn conformation (near 1693 cm^{-1}) in the spectra of either the PEO_{114}-*b*-$PBLG_{20}$ or PEO_{114}-*b*-$PBLG_{45}$ diblock copolymer. This finding is reasonable because a degree of polymerization (DP) of less than 18 for a PBLG segment results in both the α-helix and β-sheet conformations; only the rigid α-helical conformation is observed when the DP is greater than 18.[79]

To confirm the α-helical secondary structure, we recorded WAXD patterns of both the PEO-*b*-PBLG diblock copolymers at room temperature and 120 °C (Figure 3). At room temperature, the patterns featured two strong PEO diffraction peaks for the (120) and (032) planes with *d*-spacings of 0.46

https://dx.doi.org/10.1021/acs.macromol.0c01748
Macromolecules 2021, 54, 1030−1042

Table 2. BET and Raman Analyses of Microporous Carbons Templated by PEO-*b*-PBLG Diblock Copolymers

templated by resol/PEO_{114}-*b*-$PBLG_{20}$	S_{BET} (m^2/g)	S_{meso} (m^2/g)	S_{micro} (m^2/g)	V_{total} (cm^3/g)	pore size (nm)	I_D/I_G
50/50	474	67.9	406.1	0.247	1.29	0.94
60/40	478	159.0	319.0	0.208	1.20	1.07
70/30	576	142.1	433.9	0.247	1.29	0.99
resol/PEO_{114}-*b*-$PBLG_{45}$						
50/50	619	167.6	451.4	0.277	1.10	0.93
60/40	515	63.4	451.6	0.219	1.13	0.96
70/30	505	188.5	316.5	0.212	1.38	0.98

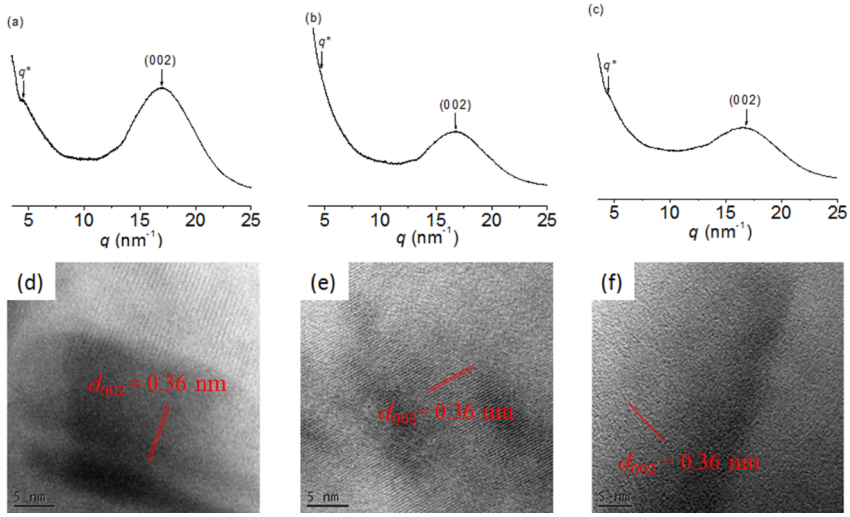

Figure 8. (a–c) WAXD patterns and (d–f) TEM images of microporous carbons obtained after calcination of resol/PEO_{114}-*b*-$PBLG_{20}$ blends at compositions of (a,d) 50/50, (b,e) 60/40, and (c,f) 70/30.

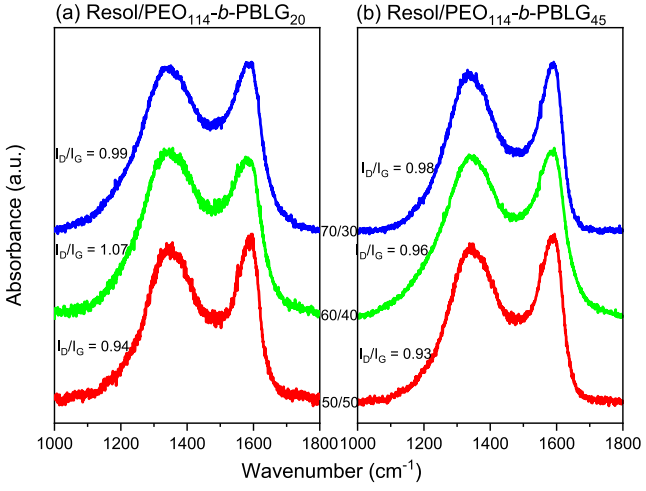

Figure 9. Raman spectra of microporous carbons obtained after calcination of (a) resol/PEO_{114}-*b*-$PBLG_{20}$ and (b) resol/PEO_{114}-*b*-$PBLG_{45}$ blends of various compositions.

and 0.32 nm, respectively (Figure 3a);[80] these two crystal peaks from the PEO segment disappeared when the temperature was higher than the melting temperature (T_m) of the PEO segment (60 °C) and the temperature for the nematic-like liquid crystal phase transition of the PBLG segment (ca. 105 °C, Figure S2), as displayed in Figure 3b. The PBLG segment displays the irreversible first order transition, which corresponds to the irreversible transition from a 7/2 to an 18/5 α-helical conformation. The higher value of q at 14.3 nm^{-1} (d = 0.44 nm) was due to the amorphous halo from the molten stage for the PEO segment; strong diffraction peaks were observed, however, at a value of q^* of 4.70 nm^{-1} (d = 1.34 nm) with a lattice parameter because of the hexagonally packed cylinder structure of the PBLG segment, based on a peak ratio of $1:\sqrt{3}:\sqrt{4}$ in this diblock copolymer, which is the solid-state modification from the nematic-like paracrystalline phase of the 18/5 α-helical conformation. As a result, both the PEO_{114}-*b*-$PBLG_{20}$ and PEO_{114}-*b*-$PBLG_{45}$ diblock copolymers featured only the α-helical conformation. FTIR and ^{1}H NMR spectra confirmed the syntheses of these PEO-*b*-PBLG diblock copolymers; GPC analyses provided their polydispersity indices; Table 1 summarizes their physical data.

Thermal and FTIR Spectral Analyses of Resol/PEO-*b*-PBLG Blends. Figure S3 presents the second heating scans of the DSC profiles of both resol/PEO_{114}-*b*-$PBLG_{20}$ and resol/PEO_{114}-*b*-$PBLG_{45}$ blends. We observed glass transition temperatures (T_g) for pure resol, pure PEO, and pure PBLG at −40, −60, and −18 °C, respectively.[78,81,82] In this case, however, because of the high crystallinity of the PEO segment, we observed only the melting temperatures (ca. 60 °C) of the PEO block segment (Figure 3a). The melting temperature of the PEO segment decreased (and ultimately disappeared) upon increasing the concentration of resol, suggesting that the OH groups of the resol interacted with the oxygen atoms of the ether units of the PEO segment to destroy their crystalline structure, as we have discussed in previous papers.[83] The T_g behavior of the PBLG segment was maintained at ca. −16 °C upon increasing resol concentration, and the resol/PEO domains displayed the highest T_g value ca. −30 °C for both resol/PEO-*b*-PBLG = 50/50 blends, which is both higher than

https://dx.doi.org/10.1021/acs.macromol.0c01748
Macromolecules 2021, 54, 1030−1042

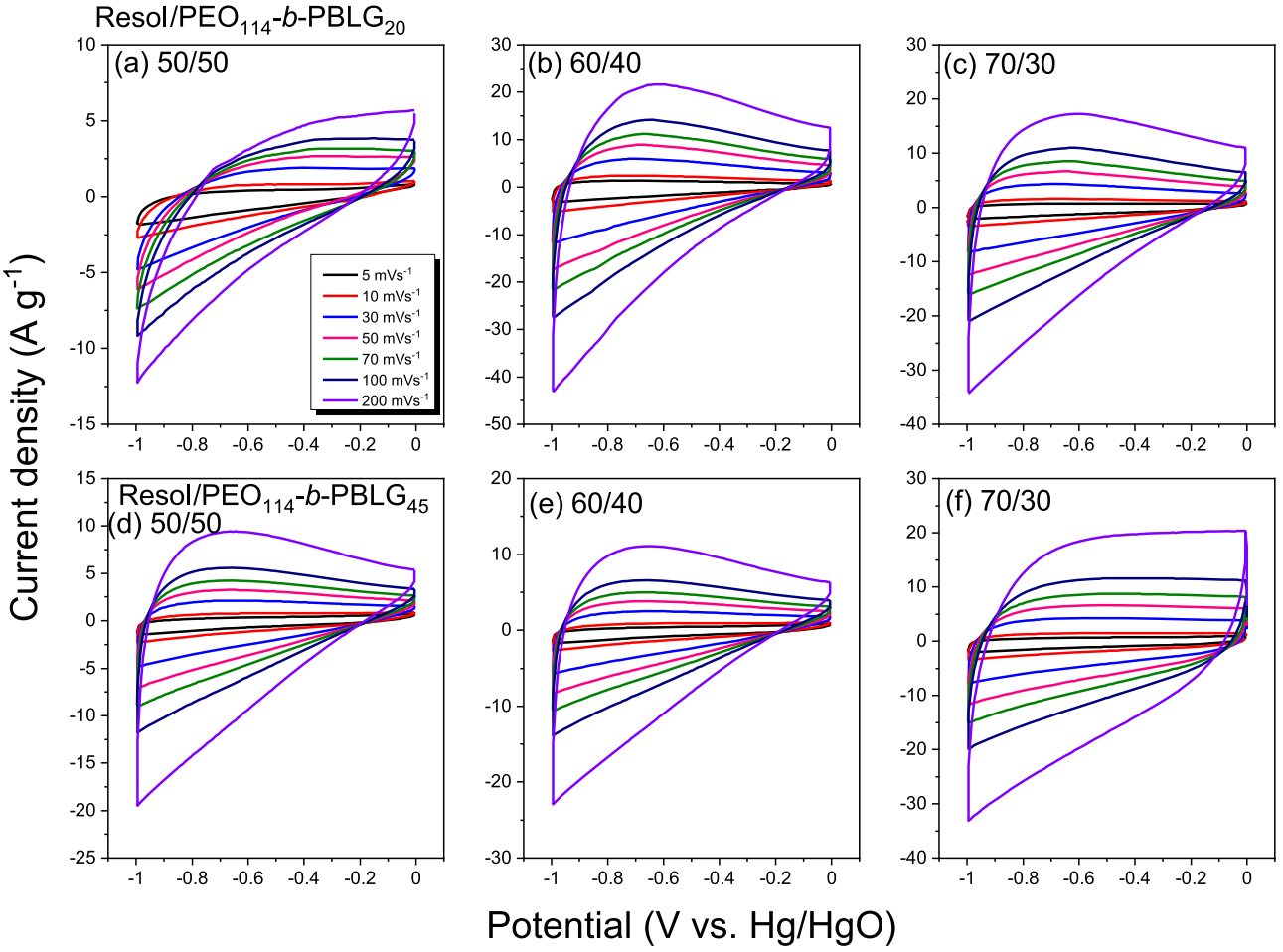

Figure 10. CV curves, recorded at various scan rates, of microporous carbons obtained after calcination of (a–c) resol/PEO_{114}-*b*-$PBLG_{20}$ blends at compositions of (a) 50/50, (b) 60/40, and (c) 70/30 and (d–f) resol/PEO_{114}-*b*-$PBLG_{45}$ blends at compositions of (d) 50/50, (e) 60/40, and (f) 70/30.

their individual block segments because of intermolecular hydrogen bonding interactions.

Figure 4 displays the FTIR spectra of various resol/PEO_{114}-*b*-$PBLG_{20}$ blends recorded at room temperature. In the absence of resol, C=O absorption signals appeared at 1652 cm^{-1} for the α-helical conformation and at 1735 cm^{-1} for the side chain C=O units of the PBLG segment (Figure 4a). These two peaks remained upon increasing the resol concentration, but we did not, however, observe any signals for intermolecular hydrogen bonding of the resol OH groups with the PBLG segment in the spectrum of the PEO-*b*-PBLG diblock copolymer—in contrast to the situation for the phenolic/PBLG binary blend system.[82] In the ether region (Figure 4b), the band at 1110 cm^{-1} for the free ether units of the PEO segment shifted to 1094 cm^{-1} (representing ether units hydrogen bonded with resol OH groups) when the resol concentration was 70 wt %. In previous studies,[82,83] we found that resol OH groups could interact through hydrogen bonding with both PEO and PBLG segments; the interassociation equilibrium constants of phenolic/PEO (K_A = 264.8)[83] and phenolic/PBLG (K_A = 9.0)[82] blends, determined using the Painter–Coleman association model,[84] implied, however, that resol OH groups prefer to interact with PEO segments over PBLG segments. As a result, in this present study, the OH groups of resol interacted with the PEO segment only and destroyed its crystal structure (thus, the signal for the melting temperature disappeared); the OH groups of resol did not interact with the PBLG segments because of the weaker intermolecular hydrogen bonding (T_g values did not change).

To further examine the behavior of the crystal structure and the α-helical conformation in these resol/PEO_{114}-*b*-$PBLG_{20}$ blend systems, we recorded their WAXD patterns at both room temperature and 120 °C (Figure 5). At room temperature, the strong PEO diffraction peaks for the (120) and (032) planes were depressed upon increasing the resol concentration, ultimately disappearing at 60 wt % resol (Figure 5a), consistent with the DSC data. At 120 °C, the α-helical conformation remained for the PBLG segment, based on a peak ratio of $1:\sqrt{3}:\sqrt{4}$, upon increasing the resol concentration (Figure 5b); thus, the α-helical conformation of the PBLG segment was stabilized through blending with resol resin, even at higher temperature. In addition, the expansion of the hexagonally packed cylinder structure of the PBLG domain upon increasing resol concentration of resol/PEO_{114}-*b*-$PBLG_{45}$ blends at 120 °C is shown in Figure S4. The *d*-spacing is increased from 1.30 to 1.33 nm upon increasing resol concentrations, indicating that resol is able to swell PBLG domains in resol/PEO_{114}-*b*-$PBLG_{45}$ blends, as shown in Scheme 2b.

Microporous Carbons Templated by PEO-*b*-PBLG Diblock Copolymers. To obtain microporous carbons templated by PEO-*b*-PBLG diblock copolymers, it was

https://dx.doi.org/10.1021/acs.macromol.0c01748
Macromolecules 2021, 54, 1030–1042

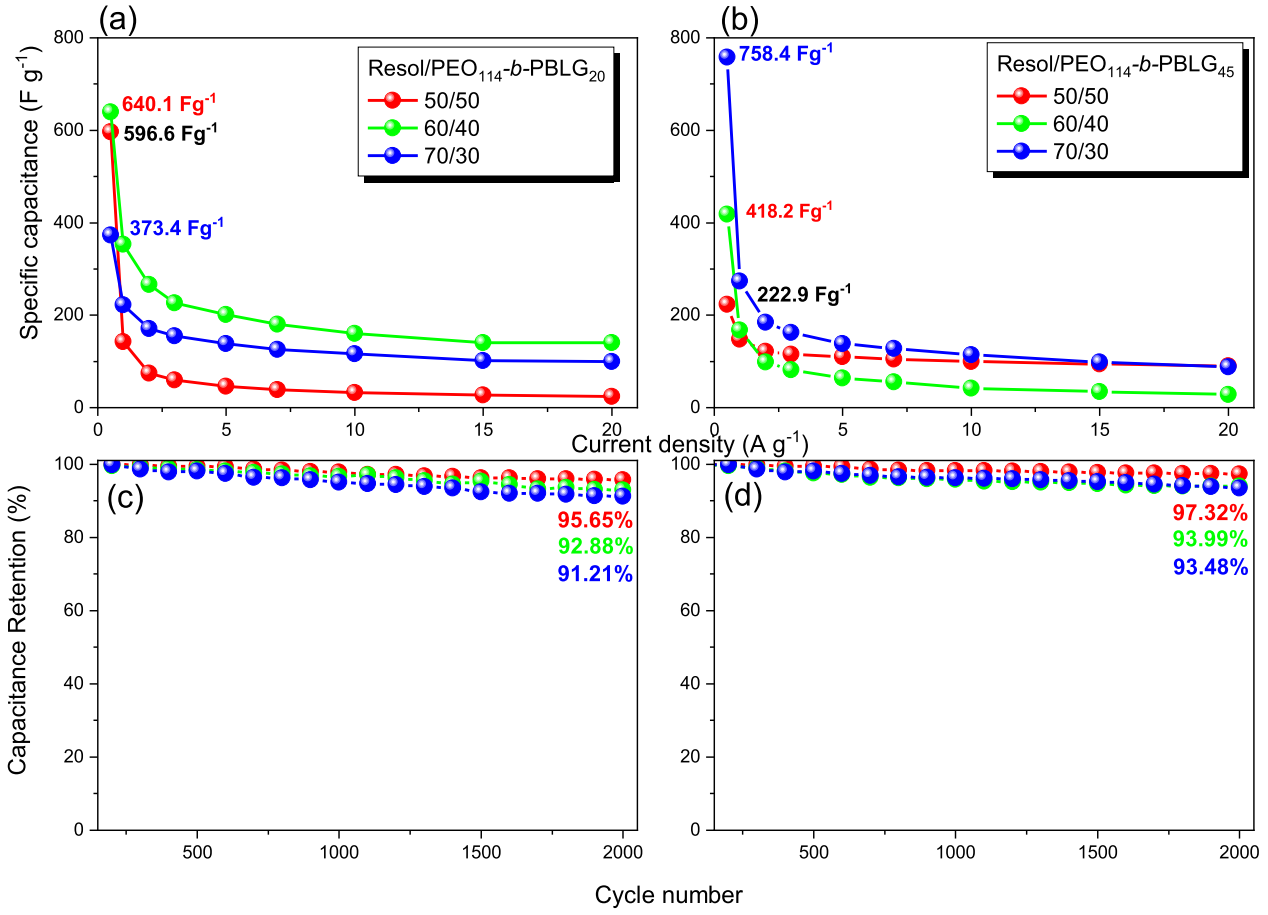

Figure 11. (a,b) Calculated capacitances at various current densities and (c,d) cycling performance measured at a current density of 10 A g^{-1} for 2000 cycles of microporous carbons obtained after calcination of (a,c) resol/PEO_{114}-*b*-$PBLG_{20}$ and (b,d) resol/PEO_{114}-*b*-$PBLG_{45}$ blends of various compositions.

necessary for us to determine a reasonable pyrolysis temperature. Thus, we performed TGA of both the resol/PEO_{114}-*b*-$PBLG_{20}$ and resol/PEO_{114}-*b*-$PBLG_{45}$ blends (Figure 6). The TGA trace of pure PEO-*b*-PBLG recorded under a N_2 atmosphere exhibited two major thermal degradation temperatures (T_d) of 330 and 415 °C corresponding to the pyrolysis temperatures of the PEO and PBLG segments, respectively. The values of T_d and char yields both increased upon increasing the resol concentration; thus, we selected a pyrolysis temperature of 420 °C and a pyrolysis time of 6 h to remove the PEO-*b*-PBLG diblock copolymer template; the microporous carbon was then obtained after further heating at 700 °C for 3 h in a tubular furnace under a N_2 atmosphere.

Figure 7 presents the N_2 sorption isotherms of the microporous carbons at 77 K. The adsorption/desorption curves of these microporous carbons were type I isotherms. A sharp rise occurred at a relatively low pressure (P/P_0 = 0−0.1), with a slight increase at intermediate pressures (P/P_0 = 0.1−0.9), and then, a sharp increase at higher pressure (P/P_0 = 0.9−1), consistent with microporous materials. For the microporous carbons templated by these two PEO-*b*-PBLG diblock copolymers, the Brunauer−Emmett−Teller (BET) surface areas ranged from 474 to 619 m^2 g^{-1}; the total pore volumes were between 0.208 and 0.277 cm^3 g^{-1}, and the pore-size distributions based on nonlocal density functional theory were 1.10 and 1.38 nm (see insets to Figure 7), as displayed in Table 2.

We used small-angle X-ray scattering (SAXS) to determine the mechanism of formation of these microporous carbons (Figure S5). All of the SAXS patterns revealed a disordered structure, with no well-defined mesoporous structure, different to those obtained when using other PEO-based diblock or triblock copolymers (e.g., PEO-*b*-PS, PEO-*b*-PCL, PPO-*b*-PEO-*b*-PPO, and PEO-*b*-PLA) as templates.[56−67] Not all PEO-based block copolymers as templates can form long-range-ordered mesoporous materials. For example, the crystallization behavior was a key factor in the synthesis of mesoporous materials templated by the block copolymer PEO-*b*-PLLA;[85] because crystallization of the PLLA segment was favored over microphase separation of the PEO-*b*-PLLA block copolymer, we had observed only the disorder lamellar mesoporous structure. Therefore, we suspected that the rigid rod of the α-helical conformation of the PBLG segments might also have favored microphase separation in the PEO-*b*-PBLG diblock copolymer; furthermore, the α-helical conformation for the PBLG segment remained after blending with resol (Figure 5b). The resol OH groups possibly interacted with both PEO and PBLG, even though we did not observe any evidence for intermolecular hydrogen bonding in the resol/PBLG domain. We did, however, observe the α-helical conformation for the PBLG segments based on FTIR spectral (Figure 4a) and WAXD (Figure 5b) analyses of the resol/PEO-*b*-PBLG blends. Figure S6 presents WAXD patterns of the resol/PEO_{114}-*b*-$PBLG_{20}$ = 60/40 blend and its correspond-

https://dx.doi.org/10.1021/acs.macromol.0c01748
Macromolecules 2021, 54, 1030−1042

ing microporous carbon obtained after thermal calcination at 700 °C. The signal for the α-helical conformation of the PBLG segments disappeared in the pattern of the microporous carbon, as expected; a broad peak appeared, however, at a value of q^* of 4.70 nm^{-1}, giving a value of d of 1.34 nm, which was presumably close to the microporous size of the carbon. As a result, we suspect that the microporous size of these porous carbons templated by PEO-*b*-PBLG block copolymers arose from the removal of the α-helical conformation of the PBLG segment (Scheme 2); thus, the microporous sizes of 1.10 and 1.38 nm, close to the strong diffraction peaks at a value of q^* of 4.70 nm^{-1}, were due to the hexagonally packed cylinder structures of the PBLG segments, as determined from the WAXD analysis. This result is similar to those of previous studies.[86−89] For example, Shantz et al. proposed that the secondary structures of templating poly(L-lysine) (PLLy) play an important role in the porous size of silica through the sol−gel process; they found that the α-helical conformation of PLLy led to cylindrical pores of approximately 1.5 nm in size, whereas larger-pore silicas resulted from the β-sheet conformation of PLLy; furthermore, grand canonical Monte Carlo simulations suggested that pores derived from the α-helical conformation of the polypeptide would have sizes between 1.3 and 1.7 nm.[86] We have also observed (Figure S3) that the amorphous halo from the resol/PEO domain (q^* = 14.3 nm^{-1}; d = 0.44 nm) shifted to a higher value of q (q^* = 17.05 nm^{-1}; d = 0.36 nm), corresponding to the (002) plane of porous carbon after thermal calcination,[90] implying the continuous removal of oxygen, hydrogen, and even carbon atoms from the resol/PEO-*b*-PBLG matrix during pyrolysis. Figure 8 displays WAXD patterns and TEM images of several selected microporous carbons; the broad peak at lower values of q correspond to microporous-sized carbon, while the signals at higher values of q represent the (002) plane of porous carbon, as presented in Figure 8a−c. Figure 8d−f displays TEM images of these microporous carbons, an interlayer spacing was approximately 0.36 nm, based on the (002) plane of the carbon structure.

We used Raman spectroscopy to examine the intrinsic properties of these microporous carbons. The intensity ratio I_D/I_G could be used to roughly calculate the degree of graphitization; the D- and G-bands appearing at 1324 and 1580 cm^{-1}, respectively, represent the sp^3- and sp^2-hybridized orbitals of the C−C bond (Figure 9). Table 2 summarizes the I_D/I_G ratios of our microporous carbons; this ratio was the highest for the microporous carbon obtained from the resol/PEO_{114}-*b*-$PBLG_{20}$ = 60/40 blend, implying a highly defected structure. Furthermore, the I_D/I_G ratios of the microporous carbons templated by PEO_{114}-*b*-$PBLG_{45}$ were lower than those templated by PEO_{114}-*b*-$PBLG_{20}$, implying that the former had less defected structures.

We used XPS to investigate the elemental contents and types in our microporous carbons. The XPS survey spectra from 0.0 to 1200 eV featured two peaks at 284 and 530 eV, corresponding to the aromatic carbon atoms of the microporous carbon skeletons and the O 1s orbitals of adsorbed H_2O, phenolic OH groups, and adsorbed O_2. In addition, the XPS survey spectra of these microporous carbons revealed that the O atom content increased upon increasing the concentration of resol in the resol/PEO-*b*-PBLG blends. The microporous carbon obtained from the resol/PEO_{114}-*b*-$PBLG_{20}$ = 70/30 blend possessed the highest O atom content (23.5%); the microporous carbons obtained from the resol/PEO_{114}-*b*-$PBLG_{20}$ = 50/50 and 60/40 blends possessed O atom contents of 17.3 and 19.9%, respectively. Similarly, the microporous carbons obtained from the resol/PEO_{114}-*b*-$PBLG_{45}$ = 50/50, 60/40, and 70/30 blends possessed O atom contents of 19.2, 24.4, and 26.1%, respectively (Table S2). Furthermore, to investigate the type of O atoms in our microporous carbon skeletons, we fitted various signals for O atoms, as shown in Figure S7; Table S2 summarizes the fitting data. The O 1s spectra of all of the microporous carbons were fitted with five peaks at 531.3, 532.3, 533.3, 534.2, and 535.9 eV representing quinone, C═O, C−O, and C−OH units, and H_2O, respectively. The fractions of the C═O, C−O, and C−OH units in all of our synthesized microporous carbons were high, reaching up to 48.59, 29.90, and 27.91%, respectively, implying that these carbons might have great potential as electrode materials for supercapacitors.

Because of their high BET surface areas, we examined the microporous carbons obtained from the resol/PEO_{114}-*b*-$PBLG_{20}$ = 50/50, 60/40, and 70/30 blends and from the resol/PEO_{114}-*b*-$PBLG_{45}$ = 50/50, 60/40, and 70/30 blends for their suitability as electrode materials for supercapacitors. We used cyclic voltammetry (CV) and galvanostatic charge−discharge (GCD) measurements in a three-electrode cell to determine the electrochemical performances of these microporous carbons. We employed a basic electrolyte of 1 M KOH to provide a wide range potential window from −1.0 to 0.0 V for the CV measurements. The CV curves of the microporous carbons obtained from the resol/PEO_{114}-*b*-$PBLG_{20}$ l(Figure 10a−c) and resol/PEO_{114}-*b*-$PBLG_{45}$ (Figure 10d−f) blends revealed the hybrid-type supercapacitor behavior of a minor pseudocapacitor (PC) and a major EDLC, originating from the O atoms in our carbon materials.[91−93] Interestingly, within the range from −1.0 to 0.0 V, the shapes of CV curves of all six of our carbon materials remain unchanged, with only the current densities increasing upon increasing the sweep rate from 5 to 200 mV s^{-1}. Figure S8 displays the GCD curves of the microporous carbons obtained from the resol/PEO_{114}-*b*-$PBLG_{20}$ (Figures S8a−c) and resol/PEO_{114}-*b*-$PBLG_{45}$ (Figures S8d−f) blends recorded at various current densities from 0.5 to 20 A g^{-1}. All of the GCD curves of these carbon materials had triangular shapes with slight bends, confirming the combination of PC and EDLC behaviors. In the case of the microporous carbons obtained from the resol/PEO_{114}-*b*-$PBLG_{20}$ blends, the discharge time of the microporous carbon from the resol/PEO_{114}-*b*-$PBLG_{20}$ = 70/30 blend was longer than that of the microporous carbons from the resol/PEO_{114}-*b*-$PBLG_{20}$ = 50/50 and 60/40 blends; in the case of microporous carbons obtained from the resol/PEO_{114}-*b*-$PBLG_{45}$ blends, the discharge times of microporous carbons from the resol/PEO_{114}-*b*-$PBLG_{45}$ = 50/50 and 60/40 blends were longer than the time of the microporous carbon from the resol/PEO_{114}-*b*-$PBLG_{45}$ = 70/30 blend. These findings suggested that we would measure high supercapacitor efficiencies for the carbons obtained from the resol/PEO_{114}-*b*-$PBLG_{20}$ = 70/30 and the resol/PEO_{114}-*b*-$PBLG_{45}$ = 50/50 and 60/40 blends. We used eq S1 to calculate the specific capacitances from the GCD curves. Figure 11a reveals that the microporous carbon obtained from the resol/PEO_{114}-*b*-$PBLG_{20}$ = 70/30 blend, at a current density of 0.5 A g^{-1} exhibited the highest specific capacitance of 758.4 F $g^{-1}$and that obtained from the resol/PEO_{114}-*b*-$PBLG_{20}$ = 50/50 and 60/40 blends had specific capacitances of 222.9 and 418.2 F g^{-1}, respectively. On the other hand, the microporous carbons obtained from the resol/

https://dx.doi.org/10.1021/acs.macromol.0c01748
Macromolecules 2021, 54, 1030−1042

PEO_{114}-*b*-$PBLG_{45}$ = 50/50 and 60/40 blends had the highest specific capacitances of 596.6 and 640.1 F g^{-1}, respectively, and those from the resol/PEO_{114}-*b*-$PBLG_{45}$ = 70/30 blend had a specific capacitance of 373.4 F g^{-1} (Figure 11b). We attribute the higher specific capacitances of the carbon materials obtained from the resol/PEO_{114}-*b*-$PBLG_{20}$ = 70/30 and resol/PEO_{114}-*b*-$PBLG_{45}$ = 50/50 and 60/40 blends to their having the highest surface areas and pore volumes, as determined from the N_2 sorption isothermal analyses. Furthermore, we examined the durability of our microporous carbon by cycling them for up to 2000 cycles under a current density of 10 A g^{-1} (Figure 11c,d). The microporous carbons obtained from the resol/PEO_{114}-*b*-$PBLG_{20}$ = 50/50, 60/40, and 70/30 blends were highly stable, retaining 95.65, 92.88, and 92.21%, respectively, of their initial capacitances (Figure 11c); likewise, the microporous carbons obtained from the resol/PEO_{114}-*b*-$PBLG_{45}$ = 50/50, 60/40, and 70/30 blends retained 97.32, 93.99, and 93.48%, respectively, of their initial capacitances (Figure 11d). These high durabilities suggest that such mesoporous carbons are promising materials for industrial energy storage applications.

CONCLUSIONS

We have synthesized two PEO-*b*-PBLG diblock copolymers through ROP of BLG-NCA when using mPEO-NH_2 as the macroinitiator. WAXD analyses confirmed that both PEO-*b*-PBLG diblock copolymers presented only the α-helical conformation, with a hexagonally packed cylinder structure, for the PBLG segment. We used FTIR spectroscopy and WAXD to determine the secondary structures, microphase separation, and self-assembled structures of PEO-*b*-PBLG after blending with various amounts of resol-type phenolic resin. FTIR spectra revealed that the resol OH groups preferred to hydrogen-bond with the ether O atoms of the PEO segment, rather than the C═O groups of the PBLG segments; WAXD revealed the increased stability of the α-helical conformation and the hexagonally packed cylinder structure of the PBLG segments after blending. We prepared microporous carbons using resol as the carbon source and our PEO-*b*-PBLG copolymers as soft templates, with a process of thermal curing followed by thermal calcination of the resol/PEO-*b*-PBLG blends. The resulting microporous carbons had high surface areas (up to 619 m^2 g^{-1}) and small pores (ca. 1.10−1.38 nm). These microporous carbons also displayed high supercapacitor capacitances (up to 758.4 F g^{-1} at a current density of 0.5 A g^{-1}) with excellent cyclic stabilities (up to 97.32% after 2000 cycles at a current density of 10 A g^{-1}). This paper provides a convenient method for the synthesis of polypeptide-based diblock copolymers that can be used as templates for the preparation of microporous carbons for electrochemical applications.

ASSOCIATED CONTENT

Supporting Information

The Supporting Information is available free of charge at https://pubs.acs.org/doi/10.1021/acs.macromol.0c01748.

Characterization of samples; electrochemical measurements of microporous carbons; and DSC thermograms and SAXS and WAXD patterns of resol/PEO-*b*-PBLG blends and the corresponding microporous carbon obtained after calcination of the resol/PEO-*b*-PBLG blend at the composition (PDF)

AUTHOR INFORMATION

Corresponding Authors

Ahmed F. M. EL-Mahdy − *Department of Materials and Optoelectronic Science, National Sun Yat-Sen University, Kaohsiung 80424, Taiwan*; Email: ahmedelmahdy@mail.nsysu.edu.tw

Shiao-Wei Kuo − *Department of Materials and Optoelectronic Science, National Sun Yat-Sen University, Kaohsiung 80424, Taiwan; Department of Medicinal and Applied Chemistry, Kaohsiung Medical University, Kaohsiung 807, Taiwan*; orcid.org/0000-0002-4306-7171; Email: kuosw@faculty.nsysu.edu.tw

Authors

Tzu Ching Yu − *Department of Materials and Optoelectronic Science, National Sun Yat-Sen University, Kaohsiung 80424, Taiwan*

Mohamed Gamal Mohamed − *Department of Materials and Optoelectronic Science, National Sun Yat-Sen University, Kaohsiung 80424, Taiwan*; orcid.org/0000-0003-0301-8372

Complete contact information is available at: https://pubs.acs.org/10.1021/acs.macromol.0c01748

Notes

The authors declare no competing financial interest.

ACKNOWLEDGMENTS

This study was supported financially by the Ministry of Science and Technology, Taiwan, under contracts MOST 108-2218-E-110-013-MY3, 108-2638-E-002-003-MY2, and 108-2221-E-110-014-MY3.

REFERENCES

(1) Wang, G.; Zhang, L.; Zhang, J. A review of electrode materials for electrochemical supercapacitors. *Chem. Soc. Rev.* **2012**, *41*, 797−828.

(2) Wei, Q.; Xiong, F.; Tan, S.; Huang, L.; Lan, E. H.; Dunn, B.; Mai, L. Energy storage: porous one-dimensional nanomaterials: design, fabrication and applications in electrochemical energy storage. *Adv. Mater.* **2017**, *29*, 1602300−1602338.

(3) Luo, Q.; Ma, H.; Hou, Q.; Li, Y.; Ren, J.; Dai, X.; Yao, Z.; Zhou, Y.; Xiang, L.; Du, H.; He, H.; Wang, N.; Jiang, K.; Lin, H.; Zhang, H.; Guo, Z. All-carbon-electrode-based endurable flexible perovskite solar cells. *Adv. Funct. Mater.* **2018**, *28*, 1706777.

(4) Sharma, S.; Soni, R.; Kurungot, S.; Asha, S. K. Naphthalene Diimide Copolymers by Direct Arylation Polycondensation as Highly Stable Supercapacitor Electrode Materials. *Macromolecules* **2018**, *51*, 954−965.

(5) Zhi, J.; Zhao, W.; Liu, X.; Chen, A.; Liu, Z.; Huang, F. Highly conductive ordered mesoporous carbon based electrodes decorated by 3D graphene and 1D silver nanowire for flexible supercapacitor. *Adv. Funct. Mater.* **2014**, *24*, 2013−2019.

(6) El-Mahdy, A. F. M.; Hung, Y. H.; Mansoure, T. H.; Yu, H. H.; Chen, T.; Kuo, S. W. A hollow microtubular triazine- and benzobisoxazole-based covalent organic framework presenting sponge-like shells that functions as a high-performance supercapacitor. *Chem.—Asian J.* **2019**, *14*, 1429−1435.

(7) Dekel, D. R. Review of cell performance in anion exchange membrane fuel cells. *J. Power Sources* **2018**, *375*, 158−169.

(8) Yarlagadda, V.; Carpenter, M. K.; Moylan, T. E.; Kukreja, R. S.; Koestner, R.; Gu, W.; Thompson, L.; Kongkanand, A. Boosting fuel cell performance with accessible carbon mesopores. *ACS Energy Lett.* **2018**, *3*, 618−621.

(9) Logeshkumar, S.; Manoharan, R. Influence of some nano-structured materials additives on the performance of lead acid battery negative electrodes. *Electrochim. Acta* **2014**, *144*, 147−153.
(10) Yolshina, L. A.; Yolshina, V. A.; Yolshin, A. N.; Plaksin, S. V. Novel lead-graphene and lead-graphite metallic composite materials for possible applications as positive electrode grid in lead-acid battery. *J. Power Sources* **2015**, *278*, 87−97.
(11) Gao, S.; Cheng, Y.-T.; Shirpour, M. Effects of cobalt deficiency on nickel-rich layered $lini_{0.8}co_{0.1}mn_{0.1}o_2$ positive electrode materials for lithium-ion batteries. *ACS Appl. Mater. Interfaces* **2019**, *11*, 982−989.
(12) Lu, J.; Lian, F.; Guan, L.; Zhang, Y.; Ding, F. Adapting FeS_2 micron particles as an electrode material for lithium-ion batteries via simultaneous construction of CNT internal networks and external cages. *J. Mater. Chem. A* **2019**, *7*, 991−997.
(13) Xu, G.; Ding, L.; Wu, T.; Xiang, M.; Yang, F. Effect of high molecular weight on pore formation and various properties of microporous membrane used for lithium-ion battery separator. *J. Polym. Res.* **2018**, *25*, 166.
(14) Hughes, M. A.; Allen, J. A.; Donne, S. W. Optimized electrolytic carbon and electrolyte systems for electrochemical capacitors. *ChemElectroChem* **2020**, *7*, 266−282.
(15) Zhang, T.; Sanguramath, R. A.; Israel, S.; Silverstein, M. S. Emulsion Templating: Porous Polymers and Beyond. *Macromolecules* **2019**, *52*, 5445−5479.
(16) He, X.; Li, X.; Ma, H.; Han, J.; Zhang, H.; Yu, C.; Xiao, N.; Qiu, J. ZnO template strategy for the synthesis of 3D interconnected graphene nanocapsules from coal tar pitch as supercapacitor electrode materials. *J. Power Sources* **2017**, *340*, 183−191.
(17) He, X.; Zhang, H.; Zhang, H.; Li, X.; Xiao, N.; Qiu, J. Direct synthesis of 3D hollow porous graphene balls from coal tar pitch for high performance supercapacitors. *J. Mater. Chem. A* **2014**, *2*, 19633−19640.
(18) Khandelwal, M.; Kumar, A. One-step chemically controlled wet synthesis of graphene nanoribbons from graphene oxide for high performance supercapacitor applications. *J. Mater. Chem. A* **2015**, *3*, 22975−22988.
(19) Pokrzywinski, J.; Keum, J. K.; Ruther, R. E.; Self, E. C.; Chi, M.; Meyer, H., III; Littrell, K. C.; Aulakh, D.; Marble, S.; Ding, J.; Wriedt, M.; Nanda, J.; Mitlin, D. Unrivaled combination of surface area and pore volume in micelle-templated carbon for supercapacitor energy storage. *J. Mater. Chem. A* **2017**, *5*, 13511−13525.
(20) Liu, Z.; Xiao, K.; Guo, H.; Ning, X.; Hu, A.; Tang, Q.; Fan, B.; Zhu, Y.; Chen, X. Nitrogen-doped worm-like graphitized hierarchical porous carbon designed for enhancing area-normalized capacitance of electrical double layer supercapacitors. *Carbon* **2017**, *117*, 163−173.
(21) Kasturi, P. R.; Ramasamy, H.; Meyrick, D.; Sung Lee, Y.; Kalai Selvan, R. Preparation of starch-based porous carbon electrode and biopolymer electrolyte for all solid-state electric double layer capacitor. *J. Colloid Interface Sci.* **2019**, *554*, 142−156.
(22) Tang, B.; Zheng, L.; Dai, X.; Chen, H. Nitrogen/oxygen co-doped porous carbons derived from a facilely-synthesized Schiff-base polymer for high-performance supercapacitor. *J. Energy Storage* **2019**, *26*, 100961.
(23) Abednatanzi, S.; Derakhshandeh, P. G.; Leus, K.; Vrielinck, H.; Callens, F.; Schmidt, J.; Savateev, A.; Van Der Voort, P. Metal-free activation of molecular oxygen by covalent triazine frameworks for selective aerobic oxidation. *Sci. Adv.* **2020**, *6*, No. eaaz2310.
(24) Zhu, T.; Yu, Q.; Ding, L.; Di, T.; Zhao, T.; Li, T.; Li, L. Atom-economical preparation of polybismaleimide-based microporous organic polymers. *Green Chem.* **2019**, *21*, 2326−2333.
(25) Chueh, C.-C.; Chen, C.-I.; Su, Y.-A.; Konnerth, H.; Gu, Y.-J.; Kung, C.-W.; Wu, K. C.-W. Harnessing MOF materials in photovoltaic devices: recent advances, challenges, and perspectives. *J. Mater. Chem. A* **2019**, *7*, 17079−17095.
(26) El-Mahdy, A. F. M.; Young, C.; Kim, J.; You, J.; Yamauchi, Y.; Kuo, S.-W. Hollow microspherical and microtubular [3+3] carbazole-based covalent organic frameworks and their gas and energy storage applications. *ACS Appl. Mater. Interfaces* **2019**, *11*, 9343−9354.
(27) El-Mahdy, A. F. M.; Hung, Y.-H.; Mansoure, T. H.; Yu, H.-H.; Hsu, Y.-S.; Wu, K. C. W.; Kuo, S.-W. Synthesis of [3+3] *β*-ketoenamine-tethered covalent organic frameworks (COFs) for high-performance supercapacitance and CO_2 storage. *J. Taiwan Inst. Chem. Eng.* **2019**, *103*, 199−208.
(28) El-Mahdy, A. F. M.; Mohamed, M. G.; Mansoure, T. H.; Yu, H.-H.; Chen, T.; Kuo, S.-W. Ultrastable tetraphenyl-p-phenylenediamine-based covalent organic frameworks as platforms for high-performance electrochemical supercapacitors. *Chem. Commun.* **2019**, *55*, 14890−14893.
(29) El-Mahdy, A. F. M.; Kuo, C.-H.; Alshehri, A.; Young, C.; Yamauchi, Y.; Kim, J.; Kuo, S.-W. Strategic design of triphenylamine- and triphenyltriazine-based two-dimensional covalent organic frameworks for CO2 uptake and energy storage. *J. Mater. Chem. A* **2018**, *6*, 19532−19541.
(30) Mohamed, M. G.; EL-Mahdy, A. F. M.; Ahmed, M. M. M.; Kuo, S. W. Direct synthesis of microporous bicarbazole-based covalent triazine frameworks for high-performance energy storage and carbon dioxide uptake. *ChemPlusChem* **2019**, *84*, 1767−1774.
(31) Abuzeid, H. R.; El-Mahdy, A. F. M.; Ahmed, M. M. M.; Kuo, S.-W. Triazine-functionalized covalent benzoxazine framework for direct synthesis of N-doped microporous carbon. *Polym. Chem.* **2019**, *10*, 6010−6020.
(32) Yang, P.; Xie, J.; Zhong, C. Biowaste-derived threedimensional porous network carbon and bioseparator for highperformance asymmetric supercapacitor. *ACS Appl. Energy Mater.* **2018**, *1*, 616−622.
(33) Tang, K.; Chang, J.; Cao, H.; Su, C.; Li, Y.; Zhang, Z.; Zhang, Y. Macropore and micropore-dominated carbon derived from poly(vinyl alcohol) and polyvinylpyrrolidone for supercapacitor and Capacitive Deionization. *ACS Sustain. Chem. Eng.* **2017**, *5*, 11324−11333.
(34) Niu, J.; Shao, R.; Liang, J.; Dou, M.; Li, Z.; Huang, Y.; Wang, F. Biomass-derived mesopore-dominant porous carbons with large specific surface area and high defect density as high performance electrode materials for Li-ion batteries and supercapacitors. *Nano Energy* **2017**, *36*, 322−330.
(35) Madito, M. J.; Matshoba, K. S.; Ochai-Ejeh, F. U.; Mongwaketsi, N.; Mtshali, C. B.; Fabiane, M.; Manyala, N. Nickel-copper graphene foam prepared by atmospheric pressure chemical vapour deposition for supercapacitor applications. *Surf. Coat. Technol.* **2020**, *383*, 125230.
(36) Bakharev, P. V.; Huang, M.; Saxena, M.; Lee, S. W.; Joo, S. H.; Park, S. O.; Dong, J.; Camacho-Mojica, D. C.; Jin, S.; Kwon, Y.; Biswal, M.; Ding, F.; Kwak, S. K.; Lee, Z.; Ruoff, R. S. Chemically induced transformation of chemical vapour deposition grown bilayer graphene into fluorinated single-layer diamond. *Nat. Nanotechnol.* **2020**, *15*, 59−66.
(37) Kong, X.; Huang, Y.; Chen, Y. Difference in formation of carbon cluster cations by laser ablation of graphene and graphene oxide. *J. Mass Spectrom.* **2012**, *47*, 523−528.
(38) Xu, J.; Gao, B.; Huo, K.-F.; Chu, P. K. Recent progress in electrode materials for nonaqueous lithium-ion capacitors. *J. Nanosci. Nanotechnol.* **2020**, *20*, 2652−2667.
(39) Liu, S.; Yin, Y.; Shen, Y.; Hui, K. S.; Chun, Y. T.; Kim, J. M.; Hui, K. N.; Zhang, L.; Jun, S. C. Phosphorus regulated cobalt oxide@nitrogen-doped carbon nanowires for flexible quasi-solid-state supercapacitors. *Small* **2020**, *16*, 1906458.
(40) Wang, H.; Gao, Q. Synthesis, characterization and energy-related applications of carbide-derived carbons obtained by the chlorination of boron carbide. *Carbon* **2009**, *47*, 820−828.
(41) Liu, T.; Liu, G. Block copolymers for supercapacitors, dielectric capacitors and batteries. *Phys. Condens. Matter.* **2019**, *31*, 233001.
(42) Chang, A. B.; Bates, F. S. The ABCc of Block Polymers. *Macromolecules* **2020**, *53*, 2765−2768.
(43) Tsou, C.-T.; Kuo, S.-W. Competing Hydrogen Bonding Interaction Creates Hierarchically Ordered Self-Assembled Structures of PMMA-b-P4VP/PVPh-b-PS Mixtures. *Macromolecules* **2019**, *52*, 8374−8383.

https://dx.doi.org/10.1021/acs.macromol.0c01748
Macromolecules 2021, 54, 1030−1042

(44) Wang, J.; Xu, Y.; Ding, B.; Chang, Z.; Zhang, X.; Yamauchi, Y.; Wu, K. C.-W. Confined Self-Assembly in Two-Dimensional Interlayer Space: Monolayered Mesoporous Carbon Nanosheets with In-Plane Orderly Arranged Mesopores and a Highly Graphitized Framework. *Angew. Chem., Int. Ed.* **2018**, *57*, 2894−2898.
(45) Tsai, C.-C.; Gan, Z.; Kuo, S.-W. Using benzoxazine chemistry and bio-based triblock copolymer to prepare functional porous polypeptide capable of efficient dye adsorption. *Polym. Chem.* **2018**, *9*, 3684−3693.
(46) Hung, W.-S.; Ahmed, M. M. M.; Mohamed, M. G.; Kuo, S. W. Competing Hydrogen Bonding Produces Mesoporous/Macroporous Carbons Templated by a High-Molecular-Weight Poly (caprolactone−b−ethylene oxide−b−caprolactone) Triblock Copolymer. *J. Polym. Res.* **2020**, *27*, 173.
(47) Lv, Y.; Zhang, F.; Dou, Y.; Zhai, Y.; Wang, J.; Liu, H.; Xia, Y.; Tu, B.; Zhao, D. A comprehensive study on KOH activation of ordered mesoporous carbons and their supercapacitor application. *J. Mater. Chem.* **2012**, *22*, 93−99.
(48) Wei, J.; Zhou, D.; Sun, Z.; Deng, Y.; Xia, Y.; Zhao, D. A Controllable synthesis of rich nitrogen-doped ordered mesoporous carbon for CO_2 capture and supercapacitors. *Adv. Funct. Mater.* **2013**, *23*, 2322−2328.
(49) Zhang, X.-Q.; Lu, A.-H.; Sun, Q.; Yu, X.-F.; Chen, J.-Y.; Li, W.-C. Unconventional synthesis of large pore ordered mesoporous carbon nanospheres for ionic liquid-based supercapacitors. *ACS Appl. Energy Mater.* **2018**, *1*, 5999−6005.
(50) Zhang, A.; Cao, S.; Zhao, Y.; Zhang, C.; Chen, A. Facile one-pot hydrothermal synthesis of particle-based nitrogen-doped carbon spheres and their supercapacitor performance. *New J. Chem.* **2018**, *42*, 6903−6909.
(51) Liu, S.; Chen, X.; Li, X.; Huo, P.; Wang, Y.; Bai, L.; Zhang, W.; Niu, M.; Li, Z. Nitrogen- and oxygen-containing micro−mesoporous carbon microspheres derived from m-aminophenol formaldehyde resin for supercapacitors with high rate performance. *RSC Adv.* **2016**, *6*, 89744−89756.
(52) Sun, Y.-N.; Sui, Z.-Y.; Li, X.; Xiao, P.-W.; Wei, Z.-X.; Han, B.-H. Nitrogen-doped porous carbons derived from polypyrrole-based aerogels for gas uptake and supercapacitors. *ACS Appl. Nano Mater.* **2018**, *1*, 609−616.
(53) Saha, D.; Li, Y.; Bi, Z.; Chen, J.; Keum, J. K.; Hensley, D. K.; Grappe, H. A.; Meyer, H. M.; Dai, S.; Paranthaman, M. P.; Naskar, A. K. Studies on supercapacitor electrode material from activated lignin-derived mesoporous carbon. *Langmuir* **2014**, *30*, 900−910.
(54) Wu, M.; Ai, P.; Tan, M.; Jiang, B.; Li, Y.; Zheng, J.; Wu, W.; Li, Z.; Zhang, Q.; He, X. Synthesis of starch-derived mesoporous carbon for electric double layer capacitor. *Chem. Eng. J.* **2014**, *245*, 166−172.
(55) Hu, Y.; Liu, H.; Ke, Q.; Wang, J. Effects of nitrogen doping on supercapacitor performance of a mesoporous carbon electrode produced by a hydrothermal soft-templating process. *J. Mater. Chem. A* **2014**, *2*, 11753−11758.
(56) Deng, Y.; Liu, J.; Liu, C.; Gu, D.; Sun, Z.; Wei, J.; Zhang, J.; Zhang, L.; Tu, B.; Zhao, D. Ultra-large-pore mesoporous carbons templated from poly(ethylene oxide)-b-polystyrene diblock copolymer by adding polystyrene homopolymer as a pore expander. *Chem. Mater.* **2008**, *20*, 7281−7286.
(57) Deng, Y.; Liu, C.; Gu, D.; Yu, T.; Tu, B.; Zhao, D. Thick wall mesoporous carbons with a large pore structure templated from a weakly hydrophobic PEO−PMMA diblock copolymer. *J. Mater. Chem.* **2008**, *18*, 91−97.
(58) Deng, Y.; Yu, T.; Wan, Y.; Shi, Y.; Meng, Y.; Gu, D.; Zhang, L.; Huang, Y.; Liu, C.; Wu, X.; Zhao, D. Ordered mesoporous silicas and carbons with large accessible pores templated from amphiphilic diblock copolymer poly(ethylene oxide)-b-polystyrene. *J. Am. Chem. Soc.* **2007**, *129*, 1690−1697.
(59) Bloch, E.; Llewellyn, P. L.; Phan, T.; Bertin, D.; Hornebecq, V. On defining a simple empirical relationship to predict the pore size of mesoporous silicas prepared from PEO-b-PS diblock copolymers. *Chem. Mater.* **2009**, *21*, 48−55.
(60) Hu, D.; Xu, Z.; Zeng, K.; Zheng, S. From self-organized Novolac resins to ordered nanoporous carbons. *Macromolecules* **2010**, *43*, 2960−2969.
(61) Chu, W.-C.; Bastakoti, B. P.; Kaneti, Y. V.; Li, J.-G.; Alamri, H. R.; Alothman, Z. A.; Yamauchi, Y.; Kuo, S.-W. Tailored design of bicontinuous gyroid mesoporous carbon and nitrogen-doped carbon from poly(ethylene oxide-b-caprolactone) diblock copolymers. *Chem.—Eur. J.* **2017**, *23*, 13734−13741.
(62) Li, J.-G.; Lin, Y.-D.; Kuo, S.-W. From microphase separation to self-organized mesoporous phenolic resin through competitive hydrogen bonding with double-crystalline diblock copolymers of poly(ethylene oxide-b-ε-caprolactone). *Macromolecules* **2011**, *44*, 9295−9309.
(63) Cao, S.; Qu, T.; Zhang, A.; Zhao, Y.; Chen, A. N-doped hierarchical porous carbon with open-ended structure for high-performance supercapacitors. *ChemElectroChem* **2019**, *6*, 1696−1703.
(64) El-Mahdy, A. F. M.; Liu, T.-E.; Kuo, S.-W. Direct synthesis of nitrogen-doped mesoporous carbons from triazine-functionalized resol for CO_2 uptake and highly efficient removal of dyes. *J. Hazard. Mater.* **2020**, *391*, 122163.
(65) Mohamed, M. G.; Hung, W.-S.; El-Mahdy, A. F. M.; Ahmed, M. M. M.; Dai, L.; Chen, T.; Kuo, S.-W. High-molecular-weight PLA-b-PEO-b-PLA triblock copolymer templated large mesoporous carbons for supercapacitors and CO_2 capture. *Polymers* **2020**, *12*, 1193.
(66) Su, W.-C.; Tsai, F.-C.; Huang, C.-F.; Dai, L.; Kuo, S.-W. Flexible epoxy resins formed by blending with the diblock copolymer PEO-b-PCL and using a hydrogen-bonding benzoxazine as the curing agent. *Polymers* **2019**, *11*, 201.
(67) Li, J. G.; Ho, Y. F.; Ahmed, M. M. M.; Liang, H. C.; Kuo, S. W. Mesoporous carbons templated by PEO-PCL block copolymers as electrode materials for supercapacitors. *Chem. Eur. J.* **2019**, *25*, 10456−10463.
(68) Shi, L.-Y.; Lee, S.; Cheng, L.-C.; Huang, H.; Liao, F.; Ran, R.; Yager, K. G.; Ross, C. A. Thin Film Self-Assembly of a Silicon-Containing Rod-Coil Liquid Crystalline Block Copolymer. *Macromolecules* **2019**, *52*, 679−689.
(69) Kotharangannagari, V. K.; Sánchez-Ferrer, A.; Ruokolainen, J.; Mezzenga, R. Thermoreversible Gel-Sol Behavior of Rod-Coil-Rod Peptide-Based Triblock Copolymers. *Macromolecules* **2012**, *45*, 1982−1990.
(70) Kopeć, M.; Yuan, R.; Gottlieb, E.; Abreu, C. M. R.; Song, Y.; Wang, Z.; Coelho, J. F. J.; Matyjaszewski, K.; Kowalewski, T. Polyacrylonitrile-b-poly(butyl acrylate) block copolymers as precursors to mesoporous nitrogen-doped carbons: synthesis and nanostructure. *Macromolecules* **2017**, *50*, 2759−2767.
(71) Tian, H.; Lin, Z.; Xu, F.; Zheng, J.; Zhuang, X.; Mai, Y.; Feng, X. Quantitative control of pore size of mesoporous carbon nanospheres through the self-assembly of diblock copolymer micelles in solution. *Small* **2016**, *12*, 3155−3163.
(72) Zhou, Z.; Liu, G. Controlling the pore size of mesoporous carbon thin films through thermal and solvent annealing. *Small* **2017**, *13*, 1603107.
(73) Ma, H.; Kim, K. T. Self-assembly of bottlebrush block copolymers into triply periodic nanostructures in a dilute solution. *Macromolecules* **2020**, *53*, 711−718.
(74) Liu, X.; Gitsov, I. Nonionic amphiphilic linear dendritic block copolymers. solvent-induced self-assembly and morphology tuning. *Macromolecules* **2019**, *52*, 5563−5573.
(75) Schmidtke, S.; Russo, P.; Nakamatsu, J.; Buyuktanir, E.; Turfan, B.; Temyanko, E.; Negulescu, I. Thermoreversible gelation of isotropic and liquid crystalline solutions of a "sticky" rodlike polymer. *Macromolecules* **2000**, *33*, 4427−4432.
(76) Barnes, B. E.; Jenkins, T. A.; Stein, L. M.; Mathers, R. T.; Wicaksana, M.; Pasquinelli, M. A.; Savin, D. A. Synthesis and characterization of a leucine-based block co-polypeptide: the effect of the leucine zipper on self-assembly. *Biomacromolecules* **2020**, *21*, 2463−2472.

https://dx.doi.org/10.1021/acs.macromol.0c01748
Macromolecules 2021, 54, 1030−1042

(77) Painter, P. C.; Tang, W. L.; Graf, J. F.; Thomson, B.; Coleman, M. M. Formation of molecular composites through hydrogen-bonding interactions. *Macromolecules* **1991**, *24*, 3929.
(78) Tsai, C.-C.; Gan, Z.; Chen, T.; Kuo, S.-W. Competitive hydrogen bonding interactions influence the secondary and hierarchical self-assembled structures of polypeptide-based triblock copolymers. *Macromolecules* **2018**, *51*, 3017−3029.
(79) Papadopoulos, P.; Floudas, G.; Klok, H. A.; Schnell, I.; Pakula, T. Self-Assembly and Dynamics of Poly(γ-benzyl-l-glutamate) Peptides. *Biomacromolecules* **2004**, *5*, 81.
(80) Chiang, Y.-W.; Hu, Y.-Y.; Li, J.-N.; Huang, S.-H.; Kuo, S.-W. Trilayered Single Crystals with Epitaxial Growth in Poly (ethylene oxide)-block-poly (ε-caprolactone)-block-poly (l-lactide) Thin Films. *Macromolecules* **2015**, *48*, 8526−8533.
(81) Kuo, S.-W.; Chen, C.-J. Functional Polystyrene Derivatives Influence the Miscibility and Helical Peptide Secondary Structures of Poly(γ-benzyl l-glutamate). *Macromolecules* **2012**, *45*, 2442−2452.
(82) Kuo, S.-W.; Chen, C.-J. Using Hydrogen-Bonding Interactions To Control the Peptide Secondary Structures and Miscibility Behavior of Poly(l-glutamate)s with Phenolic Resin. *Macromolecules* **2011**, *44*, 7315−7326.
(83) Kuo, S.-W.; Lin, C.-L.; Chang, F.-C. Phase behavior and hydrogen bonding in ternary polymer blends of phenolic resin/poly (ethylene oxide)/poly (ε-caprolactone). *Macromolecules* **2002**, *35*, 278−285.
(84) Coleman, M. M.; Graf, J. F.; Painter, P. C. *Specific Interactions and the Miscibility of Polymer Blends*; Technomic Publishing: Lancaster, PA, 1991.
(85) Altukhov, O.; Kuo, S.-W. Crystallization ability of poly(lactic acid) block segments in templating poly(ethylene oxide-b-lactic acid) diblock copolymers affects the resulting structures of mesoporous silicas. *RSC Adv.* **2015**, *5*, 22625−22637.
(86) Hawkins, K. M.; Wang, S. S.-S.; Ford, D. M.; Shantz, D. F. Poly-L-Lysine Templated Silicas: Using Polypeptide Secondary Structure to Control Oxide Pore Architectures. *J. Am. Chem. Soc.* **2004**, *126*, 9112−9119.
(87) Tomczak, M. M.; Glawe, D. D.; Drummy, L. F.; Lawrence, C. G.; Stone, M. O.; Perry, C. C.; Pochan, D. J.; Deming, T. J.; Naik, R. R. Polypeptide-Templated Synthesis of Hexagonal Silica Platelets. *J. Am. Chem. Soc.* **2005**, *127*, 12577−12582.
(88) Jia, J.; Zhou, X.; Caruso, R. A.; Antonietti, M. Synthesis of Microporous Silica Templated by Gelatin. *Chem. Lett.* **2004**, *33*, 202−203.
(89) Liu, Y.; Zhou, H.; Shen, Z.; Li, L.; Zhou, X.; Sun, P.; Yuan, Z.; Chen, T.; Li, B.; Ding, D. Synthesis of nanoporous silica with interior composite cells with synthetic block copolypeptide as template. *Chin. Sci. Bull.* **2006**, *51*, 493−497.
(90) Qu, B.; Li, C.; Zhu, C.; Wang, S.; Zhang, X.; Chen, Y. Growth of MoSe2 nanosheets with small size and expanded spaces of (002) plane on the surfaces of porous N-doped carbon nanotubes for hydrogen production. *Nanoscale* **2016**, *8*, 16886−16893.
(91) Han, J.; Zhang, L. L.; Lee, S.; Oh, J.; Lee, K.-S.; Potts, J. R.; Ji, J.; Zhao, X.; Ruoff, R. S.; Park, S. Generation of B-doped graphene nanoplatelets using a solution process and their supercapacitor applications. *ACS Nano* **2013**, *7*, 19−26.
(92) Hu, F.; Wang, J.; Hu, S.; Li, L.; Shao, W.; Qiu, J.; Lei, Z.; Deng, W.; Jian, X. Engineered fabrication of hierarchical frameworks with tuned pore structure and N,O-co-doping for high-performance supercapacitors. *ACS Appl. Mater. Interfaces* **2017**, *9*, 31940−31949.
(93) Song, S.; Ma, F.; Wu, G.; Ma, D.; Geng, W.; Wan, J. Facile self-templating large scale preparation of biomass-derived 3D hierarchical porous carbon for advanced supercapacitors. *J. Mater. Chem. A* **2015**, *3*, 18154−18162.

https://dx.doi.org/10.1021/acs.macromol.0c01748
Macromolecules 2021, 54, 1030−1042